Low frequency noise in nanoparticle-molecule networks and implications for in-materio reservoir computing

Cécile Huez, David Guérin, Florence Volatron, Anna Proust, Dominique Vuillaume

Low frequency noise in nanoparticle-molecule networks and implications for in-materio reservoir computing.

Cécile Huez,[1] David Guérin,[1] Florence Volatron,[2]
Anna Proust[2] and Dominique Vuillaume.[1*]

1) *Institute for Electronics Microelectronics and Nanotechnology (IEMN), CNRS, University of Lille, Av. Poincaré, Villeneuve d'Ascq, France.*
2) *Institut Parisien de Chimie Moléculaire (IPCM), CNRS, Sorbonne Université, 4 Place Jussieu, F-75005 Paris, France.*

** Corresponding authors: dominique.vuillaume@iemn.fr*

Abstract.

We study the low-frequency noise (LFN), *i.e.* flicker noise, also referred to as 1/f noise, in 2D networks of molecularly functionalized gold nanoparticles (NMN: nanoparticle-molecule network). We examine the noise behaviors of the NMN hosting alkyl chains (octanethiol), fatty acid oleic acids (oleylamine), redox molecule switches (polyoxometalate derivatives) or photo-isomerizable molecules (azobenzene derivatives) and we compare their 1/f noise behaviors. These noise metrics are used to evaluate which molecules are the best candidates to build in-materio reservoir computing molecular devices based on NMNs.

Introduction.

At the interface of nanostructures and bulk materials, macroscopic-scale nanostructures bridges the gap between the macroscopic and the nanoscopic material worlds. Among them, nanoparticles-molecules-networks (NMNs) are 2D arrays of molecularly functionalized nanoparticles connected on their periphery by several electrodes, which are used as a versatile platform to study the basic electron transport and optical properties in molecular electronics.[1-5] NMNs are also prone for several molecular electronics device applications, such as chemosensors, high sensitivity strain sensors, plasmonic devices, for instance.[4] Several studies have demonstrated their potentiality to implement devices for unconventional computing like reconfigurable logic gates,[6-10] neuro-inspired reservoir computing (RC).[10-12] Similar approach were also developed with atomic contacts between the nanoparticles (or nanowires in several cases) instead of molecules.[13-18] The key features to implement physical reservoir computing devices are variability, strong nonlinear response and complex dynamic interactions inside the network.[19-21] The spatiotemporal dynamics inside the RC network generate noise that can be measured at the output electrodes. The low-frequency noise (LFN or flicker noise, also referred to as 1/f noise) has a power spectral density (PSD) that scales as $1/f^n$ with f the frequency and n the frequency exponent, which is usually between 1 and 2. The n=1 case is ubiquitous and it has been observed in a large number of systems (not only electronic devices). Albeit numerous and various physical mechanisms can be at its origin, it generally occurs in electronic devices as the consequence of fluctuations of charge carriers (number of carriers, mobility fluctuations) due to any source of carrier scattering.[22-25] A more specific case, n=2, is observed for two-level fluctuations, such as burst or RTS (random telegram signal) noise when the signal randomly fluctuates abruptly between two well-defined levels. In that case, the PSD has a Lorentzian shape with a $1/f^2$ dependence above a frequency corner (and a plateau below).[23, 24, 26] Thus, a value of n close to 2 is the fingerprint

of additional and more complex noise sources in the system, likely favorable to an efficient physical RC. The two types of noise (as well as intermediate values of n) have been observed in molecular junctions (see reviews in Refs. 27, 28). In recent implementations of physical RC with various nanometarials and nanodevices, the relationship between LFN and the computational abilities of the RC was assessed with the objective to optimize the RC performances.[29, 30] While insufficient dynamics in nanomaterials or nanostructures used in physical RC can be compensated with additional external controls,[31] it is desirable to select a network with the highest complex dynamics.

Here, we compare the 1/f noise behaviors of the NMNs hosting alkyl chains (octanethiol), fatty acid oleic acids (oleylamine), redox molecule switches (polyoxometalate derivatives) or photo-isomerizable molecules (azobenzene derivatives). The first two are simple molecules used as precursors for the synthesis of NMNs (oleylamine) or as reference for comparison with already reported results (alkyl chains).[32-35] Polyoxometalates (POMs) were recently used, mixed with carbon nanotubes in a random network, to implement reservoir computing systems,[30, 36] while azobenzene derivatives are optically driven molecular switches[37-39] that were studied for reconfigurable logic circuits and reservoir computing approaches.[10] From the analysis of the 1/f noise, we conclude that highly dense NMNs with polyoxotungstates and NMNs with azobenzene-bithiophene in the *cis* isomer are the best candidates to build reservoir computing molecular devices based on NMNs.

Results.

Figure 1 shows an optical image of the 6-electrode connected NMN devices along with the 4 molecules used to functionalized the 7-8 nm in diameter gold nanoparticles (AuNPs). The NMN with oleylamine Au-NPs is the precursor system for other functionalized NMNs derived by known ligand exchange protocols (see

Methods and the Supporting Information). The 1-octanethiol chains (C_8SH for short) are used as a reference sample since they are simple molecules and for comparison with already published results for NMNs functionalized with alkylthiols.[32-35] Then we studied the noise behaviors of NMN with $(TBA^+)_3[PW_{11}O_{40}(SiC_3H_6SH)_2]^{3-}$ ($PW_{11}SH$ for short, TBA^+ is tetrabutylammonium, $[NBu_4]^+$) and azobenzene-bithiophene-butylthiol (AzBT for short). The photo-switching behavior of the AzBT molecules in a self-assembled monolayer molecular junction (MJ) was previously reported with a conductance ratio up to *ca.* $7x10^3$ between the "cis" isomer (high conductance state) and the "trans" isomer (low conductance state),[39] and a on/off conductance ratio up to *ca.* 600 in a NMN.[10, 40] Here we study the LFN behavior of the NMNs with the AzBT in the two states. For the 4 molecules, we formed 2D-NMN with a roughly hexagonal arrangement of the functionalized AuNP between the 6 electrodes (see the experimental procedure for NMN fabrication in the Supporting Information and Figs. 1b-c and S2-S4 for their characterization by SEM). Image analysis (using ImageJ)[41] shows that the AuNP size and the inter-AuNP distances are Gaussian distributed with a mean AuNP diameter between 7-8 nm (see Figs. S2-S4 in the Supporting Information). The inter-AuNP distance varies depending on the nature of the molecules, from ≈ 0.8 nm (for C_8SH-NMN) to ≈ 4.5 nm (AzBT-NMN). Table 1 summarizes these structural characterizations.

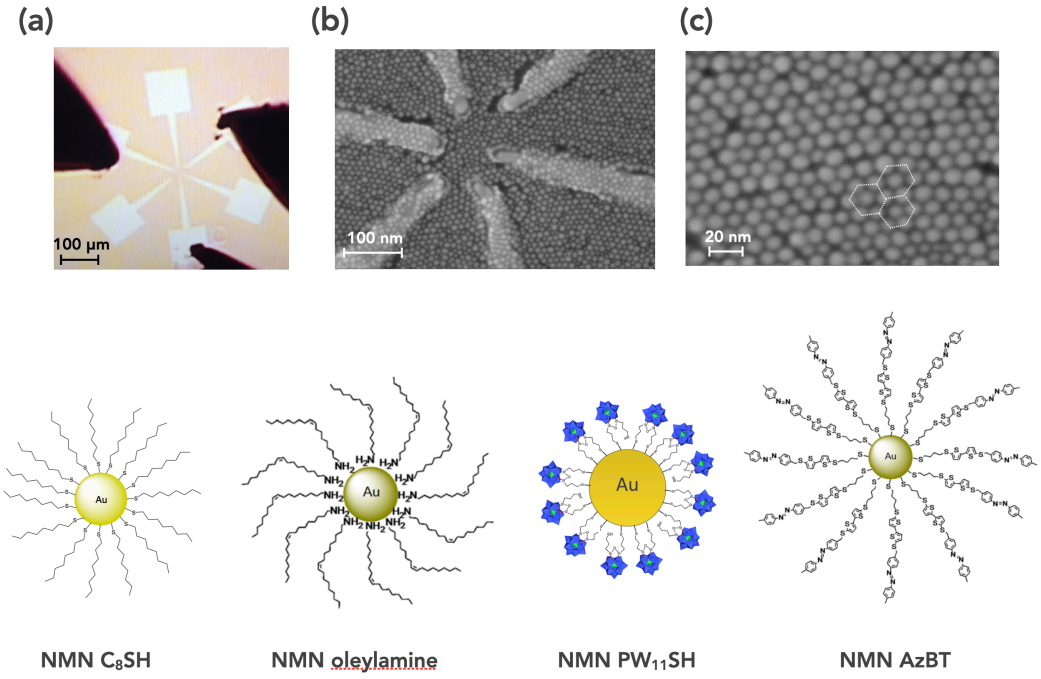

***Figure 1**. **(a)** Optical image of the NMN devices with the 6 concentric electrodes and contacting pads (the black cones are the tips of the prober). **(b and c)** Scanning electron microscope images of the NMN at different magnification (214.64k and 659.75k, respectively). The panel (b) shows the 6 electrodes, the central ring between the electrode has a diameter of ca. 100 nm. Panel (c) is a zoom near the electrodes. The hexagonal packing of the functionalized AuNP (here with $PW_{11}SH$) is illustrated by the dotted white lines in the panel (c). Schemes of the four studied systems: AuNP functionalized with C_8SH, oleylamine, $PW_{11}SH$ and AzBT, respectively (schemes not on scale). In the $PW_{11}SH$ case, the counterions (3 TBA^+ per POM) are omitted for clarity.*

	AuNPs diameter (nm)	NND (nm)	Molecule length (nm)
Oleylamine-NMN	7.8 ± 1.2	1.8 ± 0.4	2.0 [a]
C_8SH-NMN	7.8 ± 2.7	1.5 ± 0.3	1.3 [b]
PW_{11}SH-NMN	8.0 ± 1.2 (batch 1) 7.2 ± 1.6 (batch 2)	1.4 ± 0.4 (batch 1) 2.1 ± 0.7 (batch 2)	1.8 [c]
AzBT-NMN	9 ± 2 [d]	4.5 [d]	3.0 nm ("trans") [e] 2.5 nm ("cis") [e]

***Table 1**. The SEM images (Figures S2-S4) were analyzed with ImageJ[41] to obtain the statistical distribution of the AuNP diameter. The inter-nanoparticle distance was calculated with a nearest neighbor distance (NND) ImageJ plugin. The histograms (Figures S2-S4) were fit with a Gaussian distribution, the mean values and standard deviations are given in this table. The molecule lengths are taken from the following references: [a] Ref. 42, [b] Ref. 43, [c] Refs. 44, 45, [d] Ref. 40, [e] Ref. 39.*

The electrical measurements were carried out between two pairs of electrodes (PE) of the NMN randomly selected out of the 6 electrodes (Fig. 1b), see Methods. Figure 2a shows the typical current-voltage (I-V) curves measured between two PEs for a C_8SH-NMN and oleylamine-NMN (full data sets for different combinations of pairs of electrodes are shown in the Supporting Information, Fig. S5). The LFN was measured between the same two PEs and figure 2b shows the typical data for one PE of the C_8SH-NMN. The LFN is measured for applied voltages between 1.6 V and 11.2 V (by step of 1.6 V, applied using DC batteries, see Methods). The current power spectral density (PSD) $S_I(f)=\langle \delta I(t)^2 \rangle / \Delta f$ follows a $1/f^n$ law (where $\langle \delta I(t)^2 \rangle$ is the variance measured at a frequency f over a bandwidth Δf). The data sets for the other PEs of the C_8SH-NMN and the two PEs of the oleylamine-NMN are given in the Supporting Information (Fig. S6). The slope of the fits by a power law (straight lines in Fig. 2b)

allows to determine the frequency exponent n versus the applied voltage (Fig. 2c). The values of n are not dependent on the applied voltage and close to n ≈ 0.9-1 for the C_8SH-NMN (average ⟨n⟩=0.93 ± 0.18) and ≈ 1.2 for the oleylamine NMN (⟨n⟩=1.23 ± 0.10). The noise power (NoP) is plotted versus the DC current (corresponding to the applied voltage according to the I-Vs) in Fig. 2d (The NoP is the PSD, $S_I(f)$, integrated over the scanned frequency range 1-100 Hz). We found the classical behavior that NoP scales as I^2 (see discussion section).

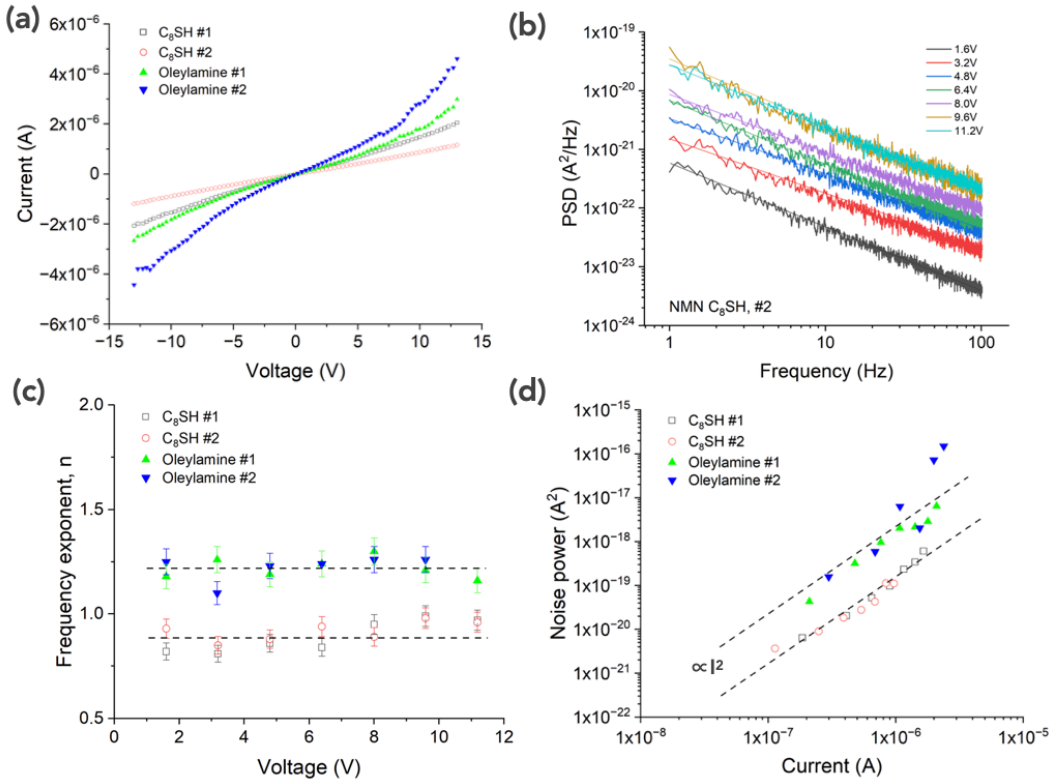

***Figure 2**. **(a)** Current-voltage (I-V) curves for the two PEs (labels #1 and #2) for the C_8SH-NMN and oleylamine-NMN. **(b)** Current power spectral density (PSD) $S_I(f)$, versus frequency for the C8SH-NMN, PE #2 measured at several applied voltages (straight lines are the fits by a power law). **(c)** Frequency exponent, n, versus the applied voltage. **(d)** Noise power (NoP, i.e. the PSD, $S_I(f)$, integrated over the scanned frequency range 1-100 Hz) versus the DC current, which is taken from the*

I-V shown in the panel (a). The dashed lines are a guide for the eyes showing the I^2 scaling.

Figures 3a-b show the I-V data set recorded for 3 different $PW_{11}SH$-NMNs (from 2 batches, see the Supporting Information) between several PEs. The three NMNs clearly differ by their level of currents, which we refer to as high current (HC, Fig. 3a), medium current (MC) and low current (LC), Fig. 3b and Fig. S7. The HC $PW_{11}SH$-NMN belongs to batch 1, while the MC and LC $PW_{11}SH$-NMNs correspond to two NMNs in the same chip from batch 2. The I-Vs of the HC $PW_{11}SH$-NMN are systematically characterized by large current instabilities for voltages (in absolute values) between *ca.* 2 and 10 V. The I-Vs for the MC and LC NMNs are more stable, we note small fluctuations at $|V| \gtrsim 10V$ for the MC NMN, while the I-Vs of the LC NMN are fully stable (Fig.S7). The LFN was measured for 2 PEs of each NMNs (in the following referred to as $PW_{11}SH$ #1 and #2 for the HC NMN of batch 1, $PW_{11}SH$ #3 and #4 for the MC NMN of batch 2 and $PW_{11}SH$ #5 and #6 for the LC NMN). Figure 3c gives the frequency exponent, n, for these samples (with the corresponding PSD data sets in the Supporting Information, Fig. S8). The main feature is higher n values ($\approx$ 1.5-1.7, $\langle n \rangle = 1.46 \pm 0.21$) for the HC NMN compared to the MC and LC NMNs for which the n values are indiscernible (randomly dispersed in the range $n \approx 0.9\text{-}1.2$, $\langle n \rangle = 1.09 \pm 0.10$). A difference is also notable in the NoP versus I behaviors (Fig. 3d). While the MC and LC NMNs follow the usual I^2 dependence, the NoPs for the HC NMNs are randomly dispersed with higher NoP values.

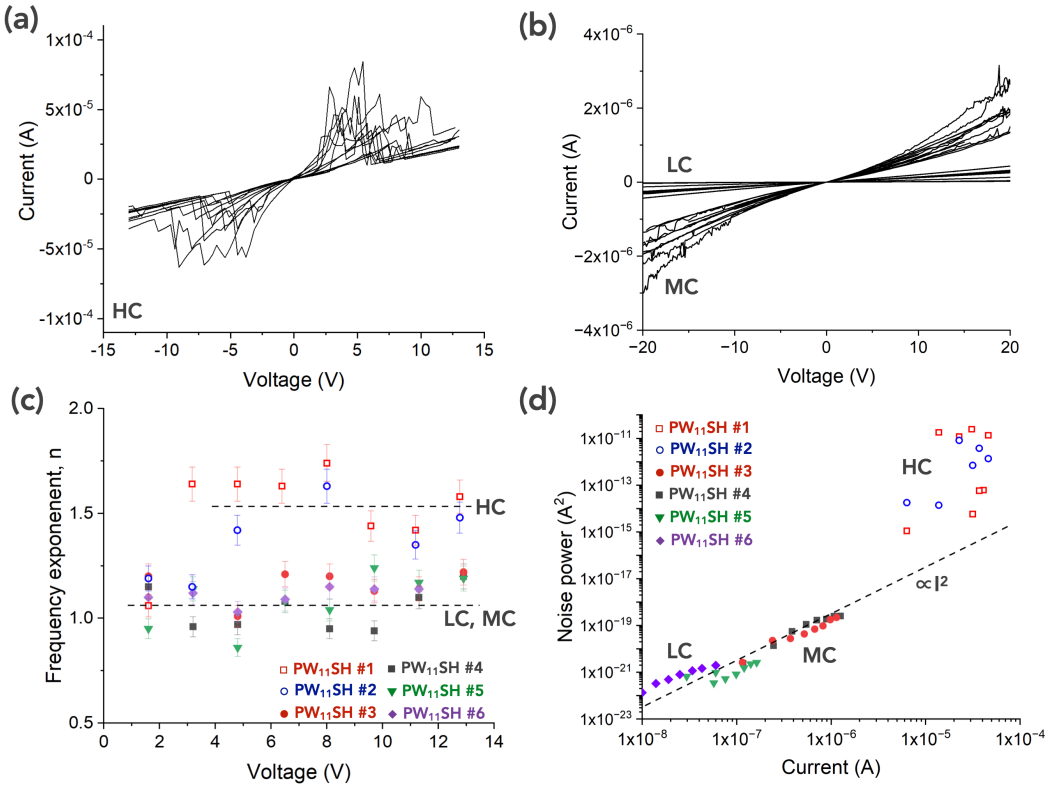

***Figure 3**. **(a)** Current-voltage (I-V) curves for the several PEs for the PW_{11}SH-NMN of batch 1. **(b)** Current-voltage (I-V) curves for the several PEs for two PW_{11}SH-NMNs of batch 2. **(c)** Frequency exponent, n, versus the applied voltage for PEs PW_{11}SH #1 and #2 for the NMN of batch 1, PW_{11}SH #3 and #4 for one NMN of batch 2 and PW_{11}SH #5 and #6 for the second one with the lowest currents. **(d)** Noise power (NoP) versus the DC current, which is taken from the I-V shown in the panel (a). The dashed line is a guide for the eyes showing the I^2 scaling. Same symbols as in panel (c).*

The same set of measurements for the AzBT-NMN devices are shown in Fig. 4 for the AzBT NMNs with the molecules in their *trans* state (initial measurements) and their *cis* state after UV light illumination (at 365 nm for 1 h). In that case, we have measured rigorously the same PE of the AzBT-NMN before and after photoisomerization to assess the change due to the AzBT isomerization in the

NMN. After the UV illumination, we clearly observed an increase of the current by a factor ≈ 15 (Fig. 4a) in agreement with our previous finding that the *cis*-AzBT NMNs are more conducting than the *trans*-AzBT NMNs.[10, 40] From the $1/f^n$ measurements (Figs. 4b), we show that the frequency exponent, n, has different behaviors for the two AzBT isomers. For the *trans* state, n increases from ca. 1 to 1.3 when increasing the applied voltage from 1 to 12 V, while for the *cis* state, it is constant to n ≈ 1.4 (⟨n⟩=1.37 ± 0.05, Fig. 4c) at all the applied voltages. The NoP scales as I^2 (Fig. 4d).

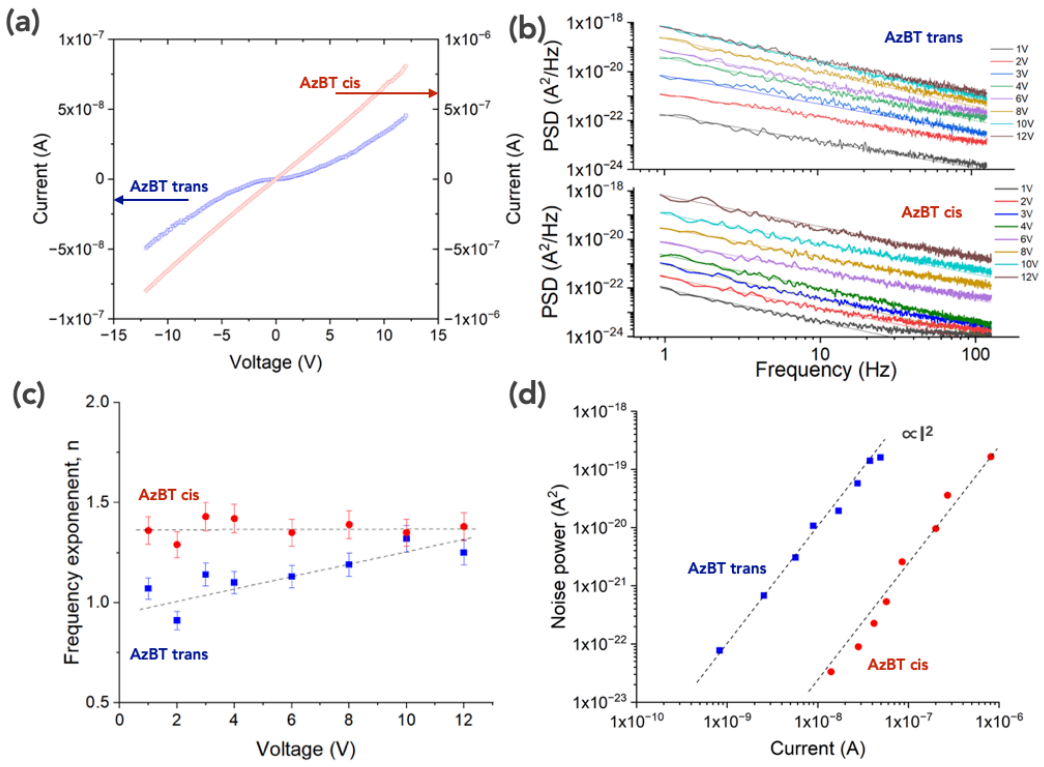

Figure 4. ***(a)*** *Current-voltage (I-V) curves for the same PE with the AzBT molecules in the trans and cis states.* ***(b)*** *Current power spectral density (PSD) $S_I(f)$, versus frequency measured at several applied voltages and for the two states of the AzBT molecules.* ***(c)*** *Frequency exponent, n, versus the applied voltage.* ***(d)*** *Noise power (NP) versus the DC current, which is taken from the I-V shown in the panel (a). The dashed lines are a guide for the eyes showing the I^2 scaling.*

Discussion.

Since the source of noise in electronic devices are multiple,[25, 46] we discuss several possible physical origins focussing on the more relevant for molecular based devices.[27, 28]

Octanethiol and oleylamine NMNs. The LFN behavior of the NMNs follows the empirical Hooge law given by[22, 25]

$$S_I(f) = \frac{\alpha_H I^2}{N f^n} \quad (1)$$

where I is the DC current, f the frequency (with a frequency exponent, n), N is the number of free carriers in the device and α_H the Hooge constant. The LFN behavior of the C_8SH-NMN is in agreement with previous reports for similar systems (AuNPs capped with alkylthiols of 8 to 12 carbon atoms)[32, 33] with n close to ≈ 1 (⟨n⟩=0.93 ± 0.18) (Fig. 2), independent of the applied voltage (or current passing through the NMNs). The frequency exponent is slightly larger, n ≈ 1.2, for the oleylamine-NMNs (⟨n⟩=1.23 ± 0.10). We also note a larger NoP in the latter case. The LFN can originate from various physical phenomena, such as conformational fluctuations of the molecules, fluctuations of the molecule-metal bonding, tiny motion of the AuNPs. It has been shown that alkyl chains have different electrical conductances whether they are in their "all trans" conformation or whether they have "gauche" defects along the chain.[47] For a long chain as oleylamine, the probability to have "gauche" defects is higher than for a shorter one as octanethiol, and thus should induce more noise fluctuators. However, in the two cases, the NDD is almost equal to the molecule size (Table 1) and consequently they are likely strongly interdigitated inside the AuNP gaps, a feature that probably minimizes this noise source. The other difference is the chemical nature of the anchoring groups (thiol versus amine). From the study of single molecule junctions (STM break junction) and DFT calculations, we know

that, at low voltages (typically few tens of mV), the amine anchoring group leads to a less dispersed conductance data set than the thiol-Au junctions,[48] thus potentially smaller fluctuations and current noise. This feature is due to the flexibility of the coupling of the N lone pair to Au. However, at higher voltages (as it is the case in NMNs), it has also been observed that the I-Vs of MJs using amine anchoring groups exhibit more instability and noise than the ones with S-Au anchors. This is due to the weaker binding strengths of amine to gold.[49] We suggest that the larger noise in the oleylamine-NMNs is mainly due to the molecule-metal interface bonding rather than by molecular conformational fluctuations of the molecule backbone itself. We notice that the oleylamine-NMNs have a slightly higher level of current than the C_8SH-NMNs (Fig 2a), albeit the NDD is larger (Table 1), which should have induced a less efficient electron transport from one AuNP to the next one through the molecules, according to the well-established exponential decrease of the off-resonant electron transport in aliphatic chain molecular junctions.[50, 51] This apparent contradiction is understood because the AuNPs network in the C_8SH-NMNs is more disordered, with a lower average density of AuNPs and more voids (see Figs. S2-S3). Consequently, the number of electron conduction pathways between the PEs though the 2D network is reduced (compared to the better organized oleylamine-NMNs), which can counterbalance the higher electron transport of the individual AuNP-molecules-AuNP due to the smaller NND for the C_8SH-NMNs.

Polyoxometalate NMNs. The I-V stability and LFN behaviors of the PW_{11}SH-NMNs depend on the level of DC current passing through the NMNs (Fig. 3). The larger currents for HC PW_{11}SH-NMNs (from batch 1) is consistent with the smaller NND (Table 1) and thus a better electron transfer between adjacent AuNPs through the molecules. The MC and LC NMNs (from batch 2) have a larger NND (Table 1). The difference between the MC and LC NMNs (two NMNs randomly selected on the batch 2 chip) can be explained considering the large dispersion of

the NND (Table 1). For the HC NMN, large instabilities of the I-V traces are systematically observed in all the I-V traces for applied voltages ≳ 2 V (in absolute value) and ≲ 10 V. These sudden and random instabilities during the voltage sweep translate into burst or RTS noise in the time domain and they are likely the origin of the larger frequency exponent (⟨n⟩=1.46 ± 0.21, Fig. 3). A pure RTS noise corresponds to a Lorentzian PSD given by[26]

$$S_I(f) \approx \frac{4I^2\tau}{1+(2\pi f\tau)^2} \qquad (2)$$

(i.e. a PSD ∝ $1/f^2$ above a corner frequency that depends on the time constant τ of the fluctuations). If the amplitude of the Lorentzian noise is of the same order as the strict flicker noise, a mix of the two can result to the observed $1/f^{1.4\text{-}1.5}$ behavior, at least for a certain frequency window. The I^2 behavior of NoP is no longer observed for the HC PW_{11}SH-NMNs (Fig. 3d). A critical current of few µA seems the condition to observe this RTS-like noise behavior with high n and large NoP (Fig. 3d). Indeed, this behavior clearly disappears when lower currents (< 0.3 µA) are passing through these HC NMNs (at low applied voltages ≤ 1 V) - Fig. S9. In these conditions, stable I-Vs are recovered, and the LFN is characterized by a frequency exponent n ≈ 1.1-1.2 (Fig. S9). Similarly, the LFN of the MC and LC NMNs (for which DC currents are ≤ 2 µA, Figs. 3b and 3d) also display the usual "1/f" behavior with ⟨n⟩=1.1 ± 0.1 (Fig. 3c) and the NoP scaling as I^2 (Fig. 3d). Since the same voltages are applied on all the NMNs, this change of the LFN behavior is current-driven, with a critical current ≳ 5 µA to induce this RTS-like $1/f^{1.4\text{-}1.5}$ noise behavior (Fig. 3d). We suggest that this RTS-like fluctuations are due to trapping/ detrapping of electrons by the POMs, which are known as efficient electron attractors.[52-54] When the electron flux though the NMN is high enough (as in HC NMNs), POMs can capture a significant number of electrons and get reduced. It is known that the electrical conductance of reduced POMs (in thin film, in self-assembled monolayer junction, as well as in single molecule junction)[52, 55, 56] is

increased (mainly due to a lowering of the LUMO). Thus, the conductance of the AuNP-POM-AuNP building blocks in the NMNs increases, and so do the global current through the NMNs. Simultaneously, the POMs become negatively charged (the number of countercations is not changed) and a strong Coulomb repulsion between the closely adjacent POMs can force detrapping of electrons from the POMs to equilibrate the electrostatic landscape in the NMNs. This trapping/detrapping dynamics leads to the RTS-like noise. When the current in the NMNs is too low, less electrons are trapped in the POMs and the competition between trapping and Coulomb detrapping is reduced. The RTS-like noise is consequently reduced in the NMNs and only flicker noise is observed in MC and LC NMNs. The voltage window (ca. $2<|V|<10$ V) where the large fluctuations are observed in the I-V curves of the HC NMNs (Fig. 3a) correspond roughly to a local voltage of 0.2 - 1 V inside a single AuNP-POMs-AuNP (considering an average number of 10 single junctions between the peripheral electrodes of the NMNs, see details in the Supporting Information). The LUMO of the POM is readily accessible within this voltage range. The redox potential (-0.43 V/SCE in acetonitrile)[57] gives a LUMO at ≈ -4.25 eV from vacuum, and considering a work function of ≈ -4.8 to -5.1 eV for the AuNPs, the LUMO is at ≈ 0.55 - 0.85 eV from the Au Fermi energy (or even smaller, since the WF of AuNPs must be weaker, especially depending on the charge states of the NPs).[58]

Since the $1/f^{1.4-1.5}$ behavior is only observed in HC NMNs, another noise contribution could come from the current crowding[59] at the nanoscale molecule-AuNP contacts and/or at the contact between the functionalized AuNPs and the nano-electrodes. Current crowding effect unavoidably appears at high local current density due to resistance mismatches and scattering of charge injections through the nanoscale contact. This current crowding effect can also increase the noise as observed in various devices.[46, 60, 61]

Finally, we also note that n ≈ 1.4-2 was observed for single molecule junctions (STM-break junction and mechanically controlled break junction) and was tentatively ascribed to conductance fluctuations due to atomic rearrangements at the molecule/metal interface.[62, 63]

Azobenzene NMNs. For the AzBT-NMNs (*cis* state), we observed a frequency exponent at around 1.4 (⟨n⟩=1.37 ± 0.05, Fig. 4). For these NMNs, the DC current is weak and the current crowding effect can be ruled out. Based on our previous molecular simulations,[40] we have demonstrated that the *cis*-AzBT molecules in the AuNP-AuNP gap have larger conformational fluctuations than the *trans*-AzBT, because the *cis*-AzBT are weakly interdigitated in the gap (or even having completely lost contact with each other), with low interactions between them. On the contrary, with the AzBT in the *trans* isomer and more molecules interdigitated, the intermolecular interactions are increased, given rise to a more stable AuNP-molecules-AuNP building block structure in the NMNs. This picture is consistent with the smaller n value for the *trans* AzBT-NMNs (Fig. 4). In this latter case, the striking feature is the increase of the frequency exponent n with the applied voltage from ca. 1 to 1.3. It is known that the *trans-cis* isomerization of azobenzene molecules can also be electrically induced by applied an electric field of 0.1-0.7 V/Å.[64, 65] We can hypothesis that such an electrically induced *trans-cis* isomerization can stochastically happen in the NMNs, inducing more conductance fluctuations and given rise to the observed increase of the frequency exponent n as increasing the applied voltages. However, in the voltage range 8-12 V (voltages at which the LFN behavior of the *trans* AzBT-NMNs tends to be similar to the one of the *cis* AzBT-NMNs), the local electric field across an individual AuNP–molecules–AuNP building-block junction in the NMNs is ≈ 1.2 - 5.3×10^{-2} V/Å (see details in the Supporting Information), far below the electric field applied in the STM experiments.[64, 65] We conclude that this electrically induced isomerization can be ruled out in our case.

Another possible physical origin of this voltage-dependent increase of noise is the interactions with vibrational modes of the AzBT molecules. Inelastic electron tunneling spectroscopy (IETS) experiments supported by theoretical (DFT) studies on single azobenzene molecules (by MCBJ) have revealed the existence of many vibrational modes in the energy range 0-0.2 eV, especially with a strong mode at ≈ 0.18 eV for the *trans* isomer and ≈ 0.2 eV for the *cis* one.[66] These vibrational modes induce inelastic scattering in the ET through the MJ and thus conductance fluctuations and noise. Increasing the voltage across the individual AuNP-molecule-AuNP in the NMN (typically up to ≈ 1 V at an external applied bias of 10 V, see the Supporting Information), more and more vibrational modes can interact with the traveling electrons in the MJ, increasing the number of conductance fluctuators and the noise feature in the overall NMN. Here, this effect is only observed for the *trans*-AzBT-NMNs since the less stable *cis*-AzBT-NMNs are already the subject of a larger noise (*vide supra*), which can hide this voltage-dependent noise effect.

Implications for physical RC. The existence of correlations between 1/f noise in a complex system and the ability of this latter to perform efficient information processing is an open question, both in biological systems and in artificial man-made neuromorphic computing.[29, 67-71] High computing capacities require complex non-linear interactions, which at the same time are also sources of noise in these systems. Some works have examined the relationship between LFN and the computational abilities of the RC, with the objective to optimize the RC performances.[29, 30] Albeit it was suggested how to overcome insufficient dynamics in emergent nanomaterials or nanostructures used for the implementation of physical RC using additional external controls,[31] it is desirable to select systems with the highest complex dynamics. On the other hand, very noisy, chaotic systems have also been suggested for computing.[72-75]

All the NMNs studied here show a large degree of variability as reflected by the dispersion of the I-V traces recorded between randomly selected PEs (*e.g.* Figs. S5 and S7). Considering a high value of the frequency exponent, n, as a fingerprint of a complex dynamic behavior whatever the physical origin of this noise, we suggest that the best candidates are PW_{11}SH-NMNs with a relatively high level of current (> few μA) and the AzBT-NMNs with the AzBT molecules in the *cis* isomer. These two systems also satisfy the condition of the nonlinearity of the NMN responses. We have previously demonstrated that *cis* AzBT-NMNs are characterized by a rich high harmonic generation (HHG), including harmonic distortion, interharmonic distortion and intermodulation distortion, as a result complex nonlinear interactions of electron transport in such a highly connected and recurrent networks of molecular junctions.[10] A similar HHG behavior is also observed for the PW_{11}SH-NMNs (Fig. S10 in the Supporting Information). Thus, we conclude that PW_{11}SH-NMNs and *cis*-AzBT-NMNs are suitable as physical reservoir computing.

Conclusions

The LFN, $1/f^n$ noise, of nanoparticle-molecule-networks (NMNs) with octanethiols and oleylamines obeys the Hooge law with a frequency exponent n close to 1 and 1.2, respectively, independent of the applied voltage. The noise amplitude scales quadratically with the DC current passing through the NMNs. The slight difference between the two NMNs is ascribed to the different molecule/gold bonding (thiol vs. amine groups). A larger frequency exponent, n ≈ 1.4-1.5 is observed for the NMNs with polyoxotungstates and *cis* isomer azobenzenes. These higher values are due to the presence of larger conductance fluctuations, like random telegraph signal, in these two NMNs. In the case of the azobenzene NMNs, this additional noise is likely due to larger molecular structure fluctuations than for the *trans* isomer. In this latter case, the frequency exponent increases (from ≈ 1 to 1.3) with the voltage. We interpret this behavior as a

consequence of the inelastic scattering of electron transport by the azobenzene vibrational modes. In the case of polyoxotungstates NMNs, we propose a current-driven stochastic redox switching of the molecules inserted between the gold nanoparticles. For a less dense NMNs with lower current, the LFN noise recovers the usual flicker noise with n close to 1. From these results, we conclude that the polyoxotungstate NMNs with the highest density of nanoparticles and NMNs with the azobenzene in the *cis* isomer are the most suitable for the implementation of in-materio reservoir computing devices.

Methods

Molecule synthesis.

1-octanethiol and (9Z)-Octadec-9-en-1-amine (oleylamine for short) were purchased from Aldrich and used as received. The AzBT derivatives were synthesized as reported in our previous work.[10, 39, 40, 76] The synthesis and characterization of $PW_{11}SH$ derivatives have been reported elsewhere.[44, 57]

Nanoparticle Molecule Network fabrication . We started with the synthesis of oleylamine-capped Au NPs as previously reported (more details in the Supporting Information).[77] The 2D NMNs were deposited on Si/SiO_2(200 nm thick) substrate equipped with the electrodes (fabricated by e-beam and liftoff, 2 nm thick Ti anchoring layer and 12 nm thick Au) by a Langmuir and transfer method according to Santhanam et al.[78] Then, we performed a ligand exchange to functionalize the NMNs with the molecules of interest (C_8SH, AzBT and $PW_{11}SH$). The fabrication of AzBT NMNs was already reported and fully characterized in our previous work.[10, 40] The full fabrication details for the C_8-NMNs and PW_{11}-NMNs are given in the Supporting Information.

Physical characterizations of the NMNs.

Scanning Electron Microscopy (Zeiss ULTRA55) was used to inspect the electrodes and NMNs (electron beam 10kV). The SEM images of NMNs were treated with ImageJ[41] to measure the size of the NPs and the inter-nanoparticle distance using the function analyze particles and the plugin NND (nearest neighbor diameter).

Electrical measurements.

The NMNs were electrically connected with a micromanipulator probe station (Suss Microtec PM-5) installed inside a glovebox (MBraun, nitrogen filled <0.1 ppm of oxygen and water vapor) to avoid any degradation of the molecules. The current-voltage (I-V) curves were acquired with an Agilent B2901A SMU (source/ measurement unit). For the noise measurements, a DC bias is applied on one of the NMN electrode by a series of 1.6 V battery or an ultra low-noise DC source (Shibasoku PA15A1 or Yokagawa 7651), the output currents are simultaneously measured on two other electrodes of the NMN by two trans-impedance amplifiers (model1211 from DL Instruments or Stanford Research Systems SR570) and analyzed by a two-channel digital signal analyzer (Agilent 35670A) in the frequency or time domains (for the $1/f^n$ noise, the reported PSD is an average done on 50 scans from 1 to 100 Hz). The noise floor of the setup is ≈ 10^{-28} A^2/Hz (measured with no sample, the prober tips raised, Fig. S11). The thermal noise of the samples is in the range ≈ 10^{-29} to 10^{-27} A^2/Hz depending on the sample resistance R according to $S_{I,th}=4kT/R$ (k the Boltzmann constant, T the temperature) . To induce the *trans-to-cis* photoisomerization of the AzBT we used a UV lamp (UVP-3UV from Analytik Jena) at a wavelength at 365 nm and a power of *ca.* 0.5mW/cm² placed at a distance of *ca.* 1cm from the sample.

Online content

Details on the NMN fabrication, scanning electron microscope images and nanoparticle size analysis, additional current-voltage and power spectral density data, high harmonic generation are available at....

Author Contributions

C.H. and D.G. fabricated the NMNs. F.V. and A.P. synthesized and characterized the PW_{11} POM. C.H. and D.V. carried out the electrical measurements. D.V. and A.P. conceived the project, supervised it and secured the project funding. The manuscript was written by D.V. with the contributions and comments of all the authors. All authors have given approval of the final version of the manuscript.

Conflicts of interest

There are no conflicts to declare.

Data availability

The data supporting this article are available from the corresponding author upon reasonable request.

Acknowledgements.

We acknowledge support of the CNRS, project "neuroPOM", under a grant of the 80PRIME program. We thank C. Boyaval (IEMN) for the SEM images.

References.

1. M. A. Mangold, C. Weiss, M. Calame and A. W. Holleitner, *Applied Physics Letters*, 2009, **94**.
2. S. J. van der Molen, J. Liao, T. Kudernac, J. S. Agustsson, L. Bernard, M. Calame, B. J. van Wees, B. L. Feringa and C. Schönenberger, *Nano Lett.*, 2009, **9**, 76-80.

3. J. F. Dayen, E. Devid, M. V. Kamalakar, D. Golubev, C. Guedon, V. Faramarzi, B. Doudin and S. J. van der Molen, *Adv Mater*, 2013, **25**, 400-404.
4. J. Liao, S. Blok, S. J. van der Molen, S. Diefenbach, A. W. Holleitner, C. Schonenberger, A. Vladyka and M. Calame, *Chem Soc Rev*, 2015, **44**, 999-1014.
5. D. Stievenard, D. Guerin, S. Lenfant, G. Leveque, C. A. Nijhuis and D. Vuillaume, *Nanoscale*, 2018, **10**, 23122-23130.
6. J. M. Tour, W. L. Van Zandt, C. P. Husband, S. M. Husband, L. S. Wilson, P. D. Franzon and D. P. Nackashi, *IEEE Transactions on Nanotechnology*, 2002, **1**, 100-109.
7. J. Skoldberg, C. Onnheim and G. Wendin, *IEEE Trans. Circuits and Systems*, 2007, **54**, 2461-2471.
8. J. Sköldberg and G. Wendin, *Nanotechnology*, 2007, **18**, 485201.
9. S. K. Bose, C. P. Lawrence, Z. Liu, K. S. Makarenko, R. M. van Damme, H. J. Broersma and W. G. van der Wiel, *Nat Nanotechnol*, 2015, **10**, 1048-1052.
10. Y. Viero, D. Guérin, A. Vladyka, F. Alibart, S. Lenfant, M. Calame and D. Vuillaume, *Advanced Functional Materials*, 2018, **28**, 1801506.
11. V. Beiu, M. Calame, G. Cuniberti, C. Gamrat, Z. Konkoli, D. Vuillaume, G. Wendin and S. Yitzchaik, *AIP conference proceedings*, 2012, **1479**, 1875-1879.
12. G. Wendin, D. Vuillaume, M. Calame, S. Yitzchaik, C. Gamrat, G. Cuniberti and V. Beiu, *International Journal of Unconventional Computing*, 2012, **8**, 325-332.
13. A. V. Avizienis, H. O. Sillin, C. Martin-Olmos, H. H. Shieh, M. Aono, A. Z. Stieg and J. K. Gimzewski, *PLoS One*, 2012, **7**, e42772.
14. H. O. Sillin, R. Aguilera, H. H. Shieh, A. V. Avizienis, M. Aono, A. Z. Stieg and J. K. Gimzewski, *Nanotechnology*, 2013, **24**, 384004.
15. E. C. Demis, R. Aguilera, H. O. Sillin, K. Scharnhorst, E. J. Sandouk, M. Aono, A. Z. Stieg and J. K. Gimzewski, *Nanotechnology*, 2015, **26**, 204003.
16. J. B. Mallinson, S. Shirai, S. K. Acharya, S. K. Bose, E. Galli and S. A. Brown, *Science Advances*, 2019, **5**, eaaw8438.
17. M. D. Pike, S. K. Bose, J. B. Mallinson, S. K. Acharya, S. Shirai, E. Galli, S. J. Weddell, P. J. Bones, M. D. Arnold and S. A. Brown, *Nano Lett*, 2020, **20**, 3935-3942.
18. J. B. Mallinson, J. K. Steel, Z. E. Heywood, S. J. Studholme, P. J. Bones and S. A. Brown, *Adv. Mater.*, 2024, 2402319.
19. W. Maass, T. Natschläger and H. Markram, *Neural Computation*, 2002, **14**, 2531-2560.
20. H. Jeager and H. Haas, *Science*, 2004, **304**, 78-80.

21. D. Verstraeten, University of Ghent, 2009.
22. F. N. Hooge, *Phys. Lett. A*, 1969, **29**, 139-140.
23. P. Dutta and P. M. Horn, *Reviews of Modern Physics*, 1981, **53**, 497-516.
24. M. B. Weissman, *Reviews of Modern Physics*, 1988, **60**, 537-571.
25. F. N. Hooge, *IEEE Transactions on Electron Devices*, 1994, **41**, 1926-1935.
26. M. J. Kirton and M. J. Uren, *Advances in Physics*, 1989, **38**, 367-468.
27. Y. Song and T. Lee, *Journal of Materials Chemistry C*, 2017, **5**, 7123-7141.
28. Y. Kim and H. Song, *App. Phys. Rev.*, 2021, **8**, 011303.
29. T. Chen, P. A. Bobbert and W. G. van der Wiel, *Small Sci.*, 2021, **1**, 2000014.
30. D. Banerjee, T. Kotooka, S. Azhari, Y. Usami, T. Ogawa, J. K. Gimzewski, H. Tamukoh and H. Tanaka, *Adv. Intell. Syst.*, 2022, **4**, 2100145.
31. S. Kan, K. Nakajima, Y. Takeshima, T. Asai, Y. Kuwahara and M. Akai-Kasaya, *Phys. Rev. Applied*, 2021, **15**, 024030.
32. C. Kurdak, J. Kim, A. Kuo, J. J. Lucido, L. A. Farina, X. Bai, M. P. Rowe and A. J. Matzger, *Appl. Phys. Lett.*, 2005, **86**, 073506.
33. W. Kruppa, M. G. Ancona, R. W. Rendell, A. W. Snow, E. E. Foos and R. Bass, *Appl. Phys. Lett.*, 2006, **88**, 053120.
34. E. L. Covington, R. W. Turner, C. Kurdak, M. P. Rowe, C. Xu and E. T. Zellers, *IEEE 2008 Sensors conference*, 2008, 102-105.
35. L. Hubble, L. Wieczorek, K. H. Müller, E. Chow, J. Cooper and B. Raguse, *IEEE 2010 International Conference on Nanoscience and Nanotechnology*, 2010, 37-40.
36. H. Tanaka, M. Akai-Kasaya, A. TermehYousefi, L. Hong, L. Fu, H. Tamukoh, D. Tanaka, T. Asai and T. Ogawa, *Nat. Commun.*, 2018, **9**, 2693.
37. N. Katsonis, M. Lubomska, M. Pollard, B. Feringa and P. Rudolf, *Prog. Surf. Sci.*, 2007, **82**, 407-434.
38. J. M. Mativetsky, G. Pace, M. Elbing, M. A. Rampi, M. Mayor and P. Samori, *J. Am. Chem. Soc.*, 2008, **130**, 9192-9193.
39. K. Smaali, S. Lenfant, S. Karpe, M. Oçafrain, P. Blanchard, D. Deresmes, S. Godey, A. Rochefort, J. Roncali and D. Vuillaume, *ACS Nano*, 2010, **4**, 2411-2421.
40. Y. Viero, G. Copie, D. Guérin, C. Krzeminski, D. Vuillaume, S. Lenfant and F. Cleri, *The Journal of Physical Chemistry C*, 2015, **119**, 21173-21183.

41. J. Schindelin, I. Arganda-Carreras, E. Frise, V. Kaynig, M. Longair, T. Pietzsch, S. Preibisch, C. Rueden, S. Saalfeld, B. Schmid, J.-Y. Tinevez, D. J. White, V. Hartenstein, K. Eliceiri, P. Tomancak and A. Cardona, *Nature Methods*, 2012, **9**, 676-682.
42. J. Borges, J. A. Ribeiro, E. M. Pereira, C. A. Carreira, C. M. Pereira and F. Silva, *J Colloid Interface Sci*, 2011, **358**, 626-634.
43. M. D. Porter, T. B. Bright, D. L. Allara and C. E. D. Chidsey, *J. Am. Chem. Soc.*, 1987, **109**, 3559-3568.
44. B. Martinez, C. Livache, E. Meriggio, X. Z. Xu, H. Cruguel, E. Lacaze, A. Proust, S. Ithurria, M. G. Silly, G. Cabailh, F. Volatron and E. Lhuillier, *The Journal of Physical Chemistry C*, 2018, **122**, 26680-26685.
45. M. Laurans, K. Trinh, K. Dalla Francesca, G. Izzet, S. Alves, E. Derat, V. Humblot, O. Pluchery, D. Vuillaume, S. Lenfant, F. Volatron and A. Proust, *ACS Appl Mater Interfaces*, 2020, **12**, 48109-48123.
46. L. K. J. Vandamme, *IEEE Transactions on Electron Devices*, 1994, **41**, 2176-2187.
47. A. Haran, D. Waldeck, R. Naaman, E. Moons and D. Cahen, *Science*, 1994, **263**, 948.
48. L. Venkataraman, J. E. Klare, I. W. Tam, C. Nuckolls, M. S. Hybertsen and M. L. Steigerwald, *Nano Lett.*, 2006, **6**, 458-462.
49. F. Chen, X. Li, J. Hihath, Z. Huang and N. J. Tao, *J. Am. Chem. Soc.*, 2006, **128**, 15874-15881.
50. B. Mann and H. Kuhn, *J. Appl. Phys.*, 1971, **42**, 4398-4405.
51. A. Salomon, D. Cahen, S. Lindsay, J. Tomfohr, V. B. Engelkes and C. D. Frisbie, *Advanced Materials*, 2003, **15**, 1881-1890.
52. O. Linnenberg, M. Moors, A. Notario-Estevez, X. Lopez, C. de Graaf, S. Peter, C. Baeumer, R. Waser and K. Y. Monakhov, *J Am Chem Soc*, 2018, **140**, 16635-16640.
53. L. Yang, J. Lei, J. M. Fan, R. M. Yuan, M. S. Zheng, J. J. Chen and Q. F. Dong, *Adv Mater*, 2021, **33**, e2005019.
54. W. Ahmad, N. Ahmad, K. Wang, S. Aftab, Y. Hou, Z. Wan, B. B. Yan, Z. Pan, H. L. Gao, C. Peung, Y. Junke, C. Liang, Z. Lu, W. Yan and M. Ling, *Adv. Sci.*, 2024, **11**, e2304120.
55. M. J. Turo, L. Chen, C. E. Moore and A. M. Schimpf, *J Am Chem Soc*, 2019, **141**, 4553-4557.
56. C. Huez, D. Guérin, S. Lenfant, F. Volatron, M. Calame, M. L. Perrin, A. Proust and D. Vuillaume, *Nanoscale*, 2022, **14**, 13790.
57. A. Gillet, S. Cher, M. Tasse, T. Blon, S. Alves, G. Izzet, B. Chaudret, A. Proust, P. Demont, F. Volatron and S. Tricard, *Nanoscale Horiz*, 2021, **6**, 271-276.

58. Y. Zhang, O. Pluchery, L. Caillard, A. F. Lamic-Humblot, S. Casale, Y. J. Chabal and M. Salmeron, *Nano Lett*, 2015, **15**, 51-55.
59. H. Murrmann and D. Widmann, *IEEE Transactions on Electron Devices*, 1969, **16**, 1022-1024.
60. A. Mercha, L. K. J. Vandamme, L. Pichon, R. Carin and O. Bonnaud, *J. Appl. Phys.*, 2001, **90**, 4019-4026.
61. P. Karnatak, T. P. Sai, S. Goswami, S. Ghatak, S. Kaushal and A. Ghosh, *Nat Commun*, 2016, **7**, 13703.
62. D. Xiang, T. Lee, Y. Kim, T. Mei and Q. Wang, *Nanoscale*, 2014, **6**, 13396-13401.
63. O. Adak, E. Rosenthal, J. Meisner, E. F. Andrade, A. N. Pasupathy, C. Nuckolls, M. S. Hybertsen and L. Venkataraman, *Nano Lett*, 2015, **15**, 4143-4149.
64. M. Alemani, M. V. Peters, S. Hecht, K.-H. Rieder, F. Moresco and L. Grill, *J Am Chem Soc*, 2006, **128**, 14446-14447.
65. M. Alemani, S. Selvanathan, F. Ample, M. V. Peters, K.-H. Rieder, F. Moresco, C. Joachim, S. Hecht and L. Grill, *J. Phys. Chem. C*, 2008, **112**, 10509-10514.
66. Y. Kim, A. Garcia-Lekue, D. Sysoiev, T. Frederiksen, U. Groth and E. Scheer, *Phys Rev Lett*, 2012, **109**, 226801.
67. M. B. John and P. Dietmar, *J. Neurosci.*, 2003, **23**, 11167.
68. D. R. Chialvo, *Nat. Phys.*, 2010, **6**, 744-750.
69. J. M. Beggs and N. Timme, *Front. Physiol.*, 2012, **3**, 163.
70. J. Hesse and T. Gross, *Front. Syst. Neurosci.*, 2014, **8**, 166.
71. T. Chen, J. van Gelder, B. van de Ven, S. V. Amitonov, B. de Wilde, H. C. Ruiz Euler, H. Broersma, P. A. Bobbert, F. A. Zwanenburg and W. G. van der Wiel, *Nature*, 2020, **577**, 341-345.
72. S. Sinha and W. L. Ditto, *Physical Review E*, 1999, **60**, 363-377.
73. S. Sinha and W. L. Ditto, *Philos Trans A Math Phys Eng Sci*, 2006, **364**, 2483-2494.
74. W. L. Ditto, K. Murali and S. Sinha, *Philos Trans A Math Phys Eng Sci*, 2008, **366**, 653-664.
75. T. Driscoll, Y. V. Pershin, D. N. Basov and M. Di Ventra, *Applied Physics A*, 2011, **102**, 885-889.
76. S. Karpe, M. Ocafrain, K. Smaali, S. Lenfant, D. Vuillaume, P. Blanchard and J. Roncali, *Chem. Commun.*, 2010, **46**, 3657-3659.
77. F. Wang, C. He, M.-Y. Han, J. Hong Wu and G. Qin Xu, *Chem. Commun.*, 2012, **48**, 6136-6138.
78. V. Santhanam, J. Liu, R. Agarwal and R. P. Andres, *Langmuir*, 2003, **19**, 7881-7887.

SUPPORTING INFORMATION

Low frequency noise in nanoparticle-molecule networks and implications for in-materio reservoir computing.

Cécile Huez,[1] David Guérin,[1] Florence Volatron,[2]
Anna Proust[2] and Dominique Vuillaume.[1*]

1) *Institute for Electronics Microelectronics and Nanotechnology (IEMN), CNRS, University of Lille, Av. Poincaré, Villeneuve d'Ascq, France.*
2) *Institut Parisien de Chimie Moléculaire (IPCM), CNRS, Sorbonne Université, 4 Place Jussieu, F-75005 Paris, France.*

** Corresponding authors: dominique.vuillaume@iemn.fr*

NMN fabrication.

Electrodes on Si/SiO₂. We used a ⟨100⟩ oriented silicon wafer covered with a 200 nm thick silicon dioxide thermally grown at 1100 °C during 135 min in a dry oxygen flow (2 L/min) and followed by a postoxidation annealing at 900 °C during 30 min under a nitrogen flow (2 L/min) to reduce the density of defects into the oxide and at the Si/SiO_2 interface. The metal electrodes were fabricated by e-beam lithography. We used a 45 nm-thick PMMA (4% 950 K, diluted with anisole with a 5:3 ratio), with an acceleration voltage of 100 keV and an optimized electron beam dose of 370 μC/cm² for the writing. After the resist development (MIBK:IPA 1:3 during 1 min and rinsed with IPA), a metallic layer (2 nm of titanium and 12 nm of gold) was deposited by e-beam evaporation followed by

the liftoff process using remover SVCTM14 during 5 h at 80 °C. We obtained well defined 6 coplanar electrodes arranged around a ring with a diameter between 80 to 120 nm.

Synthesis of molecularly functionalized AuNPs and deposition on a substrate. To better control the size of gold nanoparticles (≈10 nm), we decided to prepare oleylamine-coated AuNPs by a phase transfer protocol[1, 2] from citrate-coated AuNPs instead of the direct reduction[3, 4] of tetrachloroauric salt with oleylamine (Fig. S1). First of all, a 100 mL aqueous solution of 10 nm citrate-AuNPs was obtained following the Turkevich method.[5] A solution with 1 mL of tetrachloroauric acid trihydrate $HAuCl_4.3H_2O$ (1%) in 79 mL of deionized water was prepared. Then a 20 mL reducing solution with 4 mL of trisodium citrate dihydrate (1%) and 80 µL of tannic acid (1%) in 16 mL of deionized water was added rapidly to the Au solution under vigorous stirring (important : both solutions were mixed at 60 °C). The mixture was boiled for 10 min before being cooled down to room temperature. A continuous stirring was applied throughout the process. Then, the 100 mL solution of citrate-AuNPs was extracted with 20 mL of hexane containing 0.2 mL of oleylamine. After vigorous stirring, in a separatory funnel, the organic phase was isolated and washed twice with deionized water. The dark red suspension was distributed in centrifuge tubes and then added with 50 to 70% ethanol until the beginning of the agglomeration (purple shift). After centrifugation at 7000 rpm for 5 min, the precipitate was washed with absolute ethanol then redispersed in hexane. The washing of the AuNPs by precipitation with ethanol then redispersion in hexane was repeated twice in order to eliminate the excess of oleylamine. The AuNPs suspension is stable in hexane or toluene. It is stored in the refrigerator.

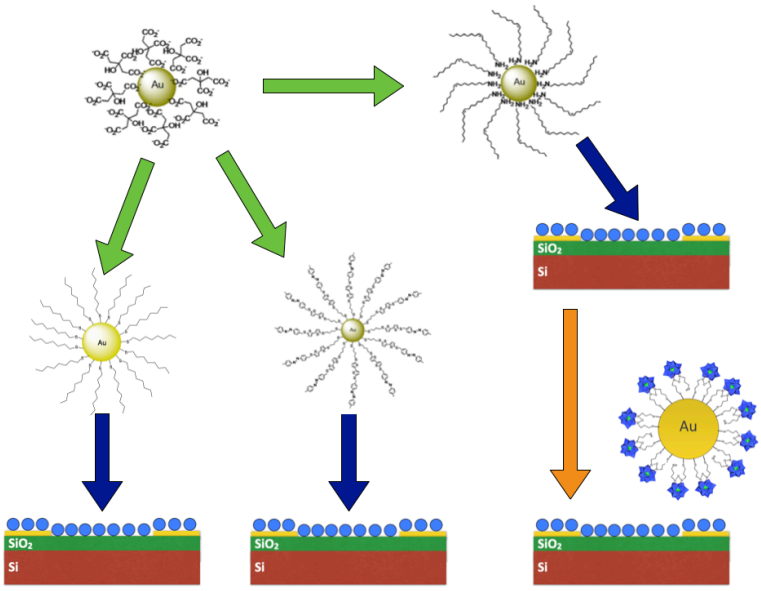

Figure S1. *Scheme of the NMN synthesis routes. The green arrows stand for ligand exchange in solution, the blue arrows indicate the transfer printing method and the orange one represents the on-surface ligand exchange (see text for details). In the case of POMs, the counterions (3 TBA⁺ per POM) are omitted for clarity*.

The next step is to form a compact 2D network of the AuNPs at the surface of the Si/SiO_2 substrate with patterned electrodes (Fig. S1, blue arrow). We used the Santhanam[6] method to form a Langmuir film at the surface of a non-miscible and non-volatile solvent. Water and ethylene glycol meet these criteria but we have obtained better quality films with ethylene glycol. In a crystallizer, we put a pierced Teflon Petri dish (hole diameter: 2 cm) upside down. We add ethylene glycol (EG) until we form a meniscus on the hole and then we spread some drops of the solution of AuNPs. We protect the assembly by covering with a crystallizer and wait around 10 minutes that the solvent evaporates and the film is self-organized on the EG surface. Then, we used a polydimethylsiloxane (PDMS)

stamp to collect the AuNP films and transfer it on the surface of the SiO_2/ electrode substrate, following the Langmuir–Schaefer technique.[7] We delicately put the PDMS stamp on the surface of the meniscus, dry the stamp under nitrogen flow and we recover the SiO_2/electrode substrate with this modified stamp. We take it out after a few seconds to be sure that the network of oleylamine-AuNPs is well transferred and we rinse quickly with ethanol the functionalized substrate. The film peels off easily from the PDMS tab. Then, we check the homogeneity and organization of the film by scanning electron microscopy (SEM), Fig.S2. We clearly observed the deposition of a monolayer of oleylamine-AuNPs with mainly a roughly hexagonal arrangement of the AuNPs and an almost homogeneous size of AuNPs. The zoom images were treated with ImageJ[8] to give us statistical data of the AuNP diameter (we used the Feret's diameter) and the inter-nanoparticle distance was calculated with a nearest neighbor distance (NND) ImageJ plugin.

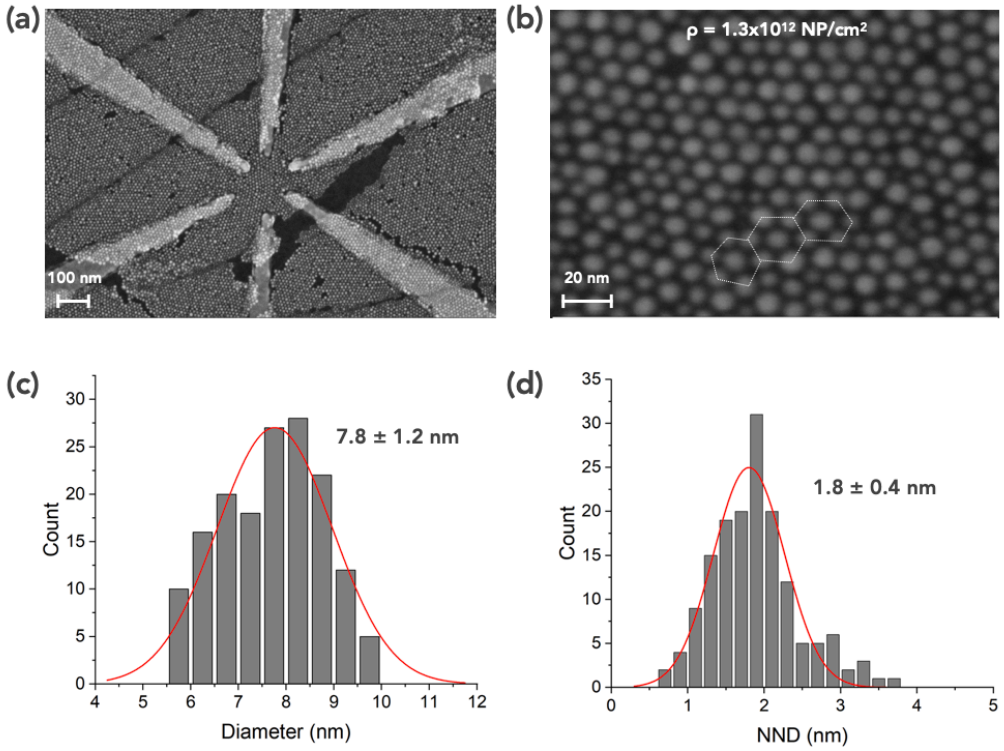

***Figure S2**. **(a-b)** Scanning electron microscope images of the oleylamine-NMN at different magnifications (82.06k and 648.56k, respectively). The panel (a) shows the 6 electrodes and the monolayer of AuNPs, the central ring between the electrode has a diameter of ca. 100 nm. Panel (b) is a zoom near the electrodes. The roughly hexagonal packing of the functionalized AuNP is illustrated by the dotted white lines in the panel (b). **(c-d)** Histograms of the AuNP diameter and nearest neighbor distance (NND), respectively. The red lines are Gaussian fits, the mean values and standard deviations are given in the figures.*

Figure S2 shows the distribution of the diameter of the AuNPs, the mean diameter is around 7.8 nm. The nearest neighbor distance (NND) is around 1.8 nm. The length of the oleylamine is ca. 2.0 nm[9] indicating that the ligands are

strongly interdigitated and folded (likely at the double bond) in the gap between two neighboring AuNPs.

Ligand exchange. The last step is the ligand exchange to replace the capping ligands (citrate or oleylamine) with the thiolated molecules (C_8SH, AzBT, $PW_{11}SH$), the thiol-ligand exchange was already demonstrated elsewhere.[10, 11] Transfer of citrate-AuNPs in organic medium was necessary for the thiolation reaction with C_8SH (Fig. S1). To this end, the 100 mL citrate-AuNPs solution was centrifuged at 13000 rpm for 30 min to eliminate the maximum of water supernatant. Then NPs were precipitated by the addition of an excess of ethanol and centrifugation at 10000 rpm for 5 min. After removal of the solvent, the black precipitate physisorbed on the centrifugation tube (attention, do not dry the precipitate!) was redispersed in 10 mL of absolute ethanol by sonication, providing a dark blue suspension immediately treated with 100 µL of octanethiol. The solution quickly turns red-purple but the thiolation is continued 24h at RT protected from air and light. The resulting black precipitate was washed 3 times with ethanol at low speed centrifugation (2000 rpm max), then redispersed by sonication in $CHCl_3$ for the preparation of MNMs.

The same method was used for the synthesis of AzBT-AuNPs as already described in a previous work.[4]

We also tried to apply this method to prepare a suspension of $PW_{11}SH$-AuNPs in organic medium but it was not possible to obtain NMN films by the Langmuir technique. To get around the problem, for the preparation of $PW_{11}SH$-NMNs we opted for a ligand exchange method on a preformed AuNPs network (Fig. S1, orange arrow). To this end, we immersed the oleylamine-NMN substrate (SiO_2 with electrodes) in a 10^{-3} M solution of $PW_{11}SH$ in acetonitrile during 5-10

minutes. Then the substrate was rinsed quickly with acetonitrile and it was dried under nitrogen flow.

Figure S3 shows the SEM characterization of the C_8SH-NMNs. The mean AuNP diameter is still 7.8 nm, but a tail at larger sizes indicates that some AuNPs are aggregated. The mean NND distance is 1.5 nm which indicates that the C8 alkyl chains (length of ca. 1.3 nm in their all-trans conformation) are strongly interdigitated and/or folded with the presence of gauche defects. We also observe a tail of the NND at larger sizes, which is due to presence of numerous voids in the layer as visible in the SEM images.

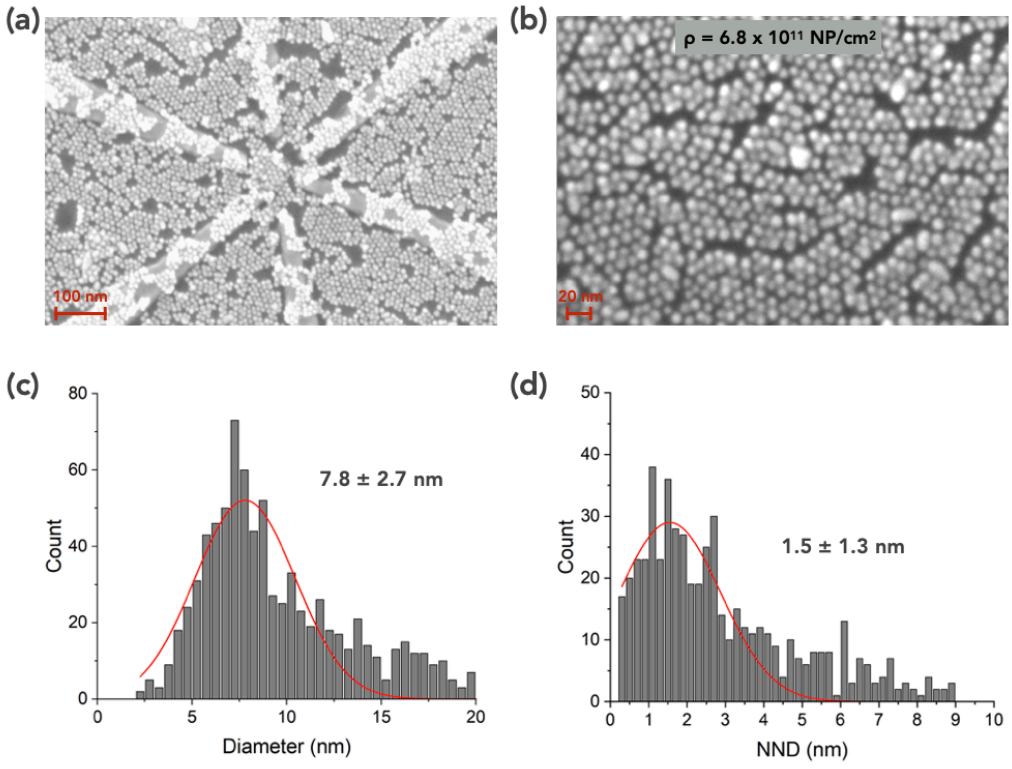

Figure S3. (a-b) *Scanning electron microscope images of the C_8SH-NMN at different magnifications (132.41k and 279.91k, respectively). The panel (a) shows the 6 electrodes and the monolayer of C8-AuNPs, the central ring between the*

electrode has a diameter of ca. 100 nm. Panel (b) is a zoom near the electrodes. ***(c-d)*** *Histograms of the AuNP diameter and nearest neighbor distance (NND), respectively. The red lines are Gaussian fits, the mean values and standard deviations are given in the figures.*

We prepared two batches of the $PW_{11}SH$-NMN, which have a slightly different organization of the nanoparticles (NPs) in the NMN (Fig. S4). For batch 1 the NPs are slightly denser than for the batch 2 (Fig. S4a and S4b, respectively). Figure 1 (main text) and Fig. S4a show the SEM images of the $PW_{11}SH$-NMNs after the on-surface ligand exchange (batch 1). We still have a 2D monolayer of AuNPs and the organization of the AuNPs looks stable after the exchange and we still observed a hexagonal packing. From the image analysis (Fig. S4c), the mean AuNP diameter is in the range 7-8 nm. The NND is slightly larger and more dispersed for the batch 2 (Fig. S4e and S4f). Compared to the size of the $PW_{11}SH$ molecule (≈ 1.8 nm, see Table 1 main text, or even a bit less since the short alkylthiol legs are flexible), we assume that no more than one layer of POMs is surrounding the AuNPs and intercalated in the gap between two adjacent AuNPs.

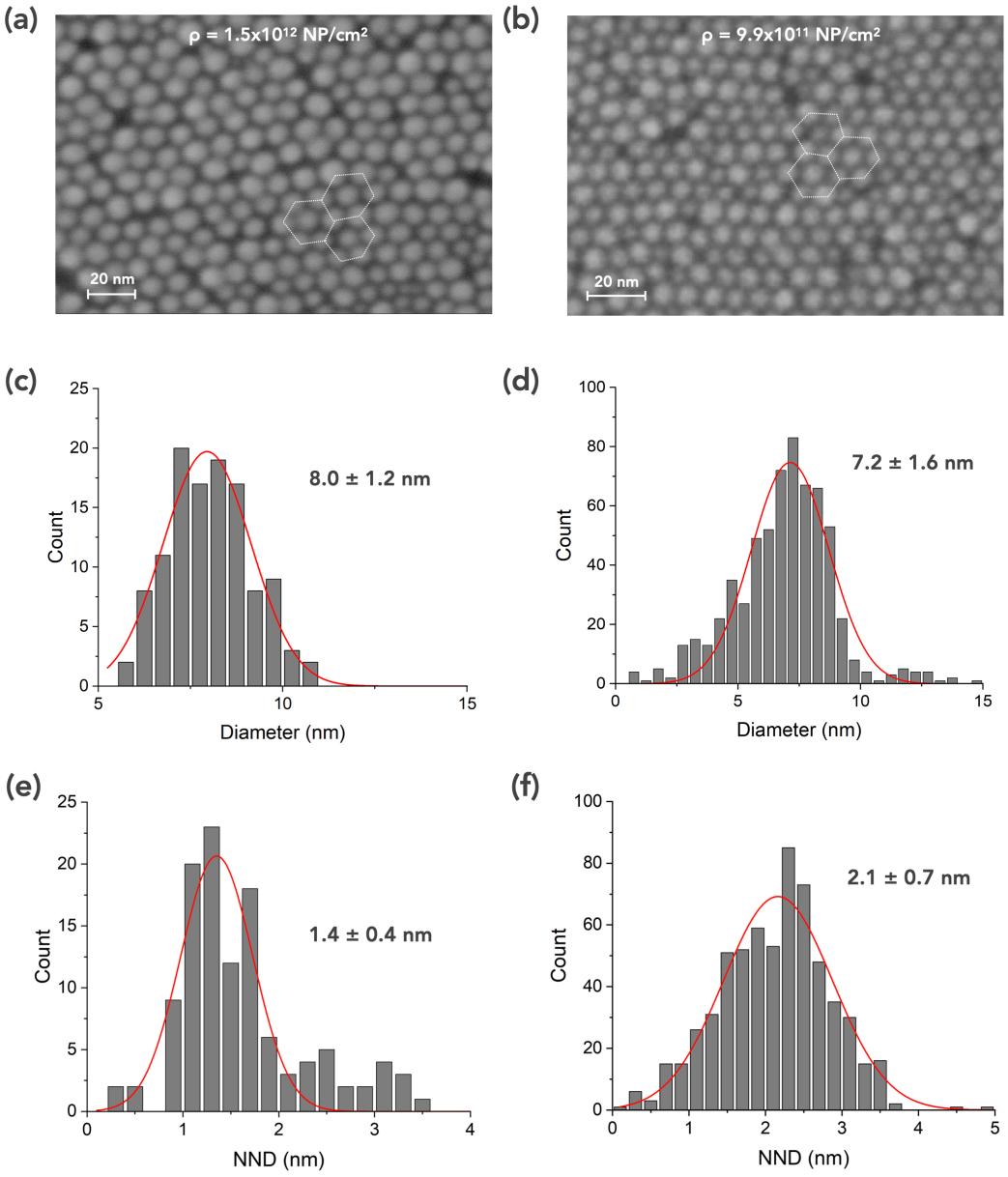

***Figure S4**. **(a-b)** Scanning electron microscope images of the PW_{11}SH-NMN for batches 1 and 2 (magnification 652.75k and 162.96k, respectively). The hexagonal packing of the functionalized AuNP is illustrated by the dotted white lines in the panel. **(c-d)** Histograms of the AuNP diameter for the NMNs of batch 1 and batch 2, respectively. **(e-f)** Histograms of the nearest neighbor distance*

(NND) for batch 1 and batch 2, respectively. The red lines are Gaussian fits, the mean values and standard deviations are given in the figures.

For the AzBT-NMN, the mean AuNP diameter was 9 nm with a mean NND of 4.5 nm as fully characterized in our previous works.[4, 12]

Estimation of the voltage inside a single AuNP-molecule-AuNP

The voltage across an individual AuNP–molecules–AuNP building block junction in the NMNs is roughly approximated by the applied voltage divided by the number of such junctions in series between the PEs (≈5 to 15 as estimated from the SEM images for the NMN with a central diameter of ≈ 100 nm and depending on whether the PEs are diametrically located of side-by-side). For a crude estimate, we can consider that on average *ca.* one tens of the external applied voltage is sustained by single AuNP-molecule-AuNP building block.

In the case of the AzBT-NMNs (see Fig. 3a in Ref. 12), in the voltage range 8-12 V (voltages at which the LFN behavior of the *trans* AzBT-NMNs tends to be similar to the one of the *cis* AzBT-NMNs) and considering an average inter-nanoparticle distance of ≈ 4.5 nm (Table 1, Ref. 4), the electric field in an individual AuNP–AzBT–AuNP junction is ≈ 1.2-5.3x10^{-2} V/Å.

Additional data.

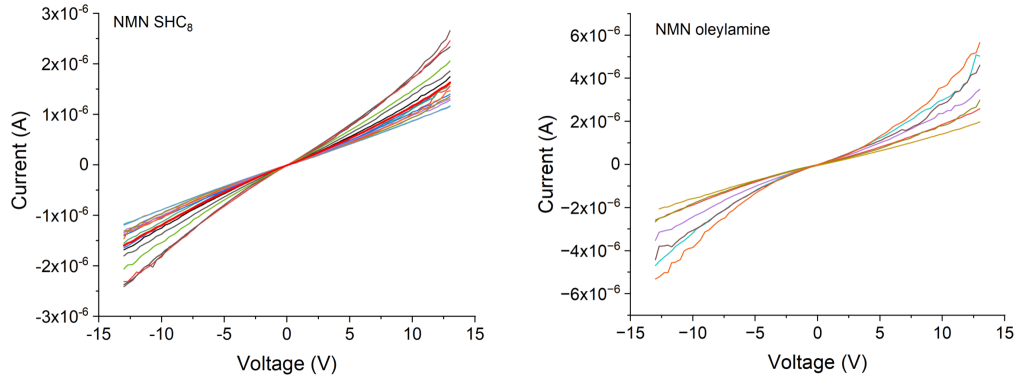

***Figure S5**. Current-voltage (I-V) curves recorded for several pairs of electrodes (PEs) of the C_8SH-NMN and oleylamine NMN.*

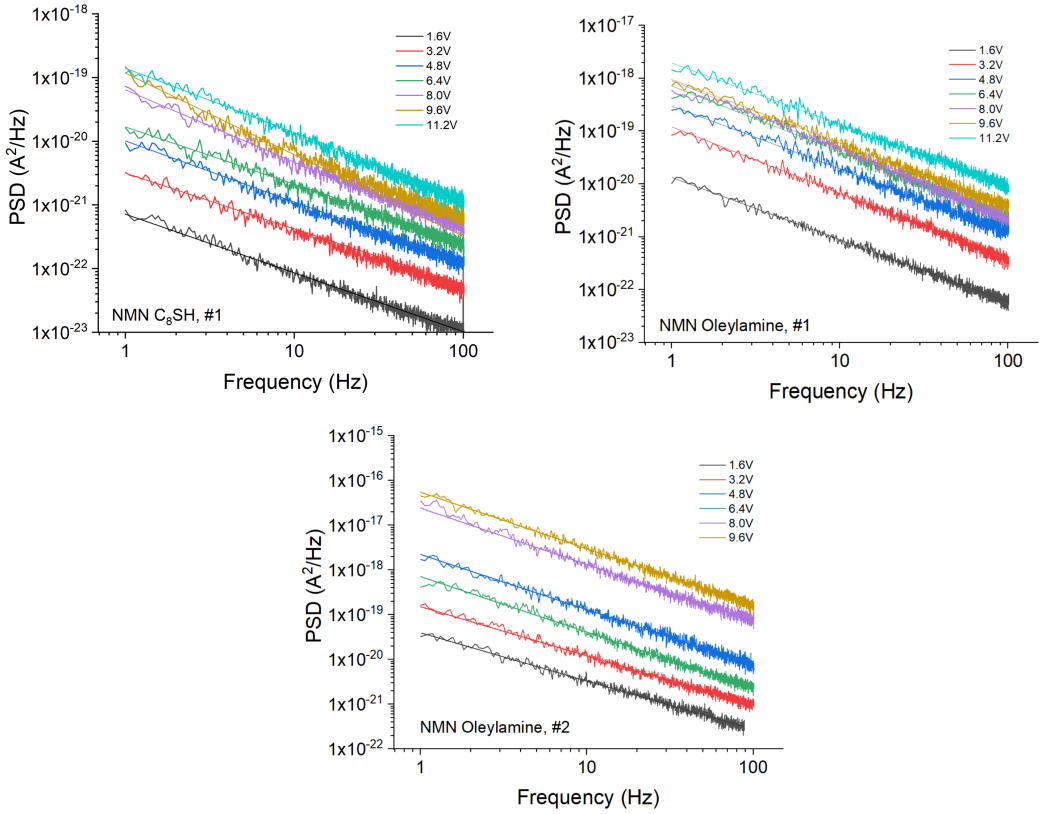

***Figure S6**. Current power spectral density (PSD), $S_I(f)$, versus frequency for the C_8SH-NMN, PE #1, and the two PEs of the oleylamine-NMN, measured at several applied voltages.*

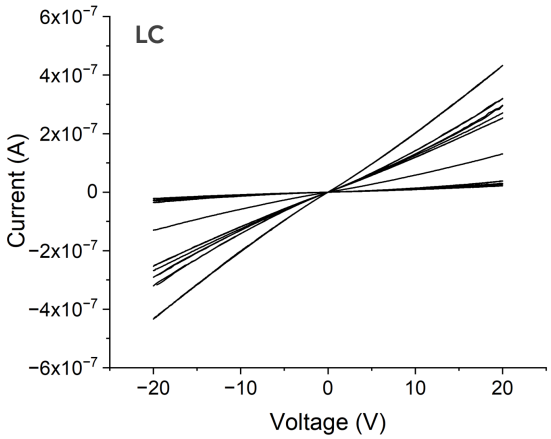

***Figure S7**. Current-voltage traces of the LC PW_{11}SH-NMN (zoom on data from Fig. 3B, main text)*

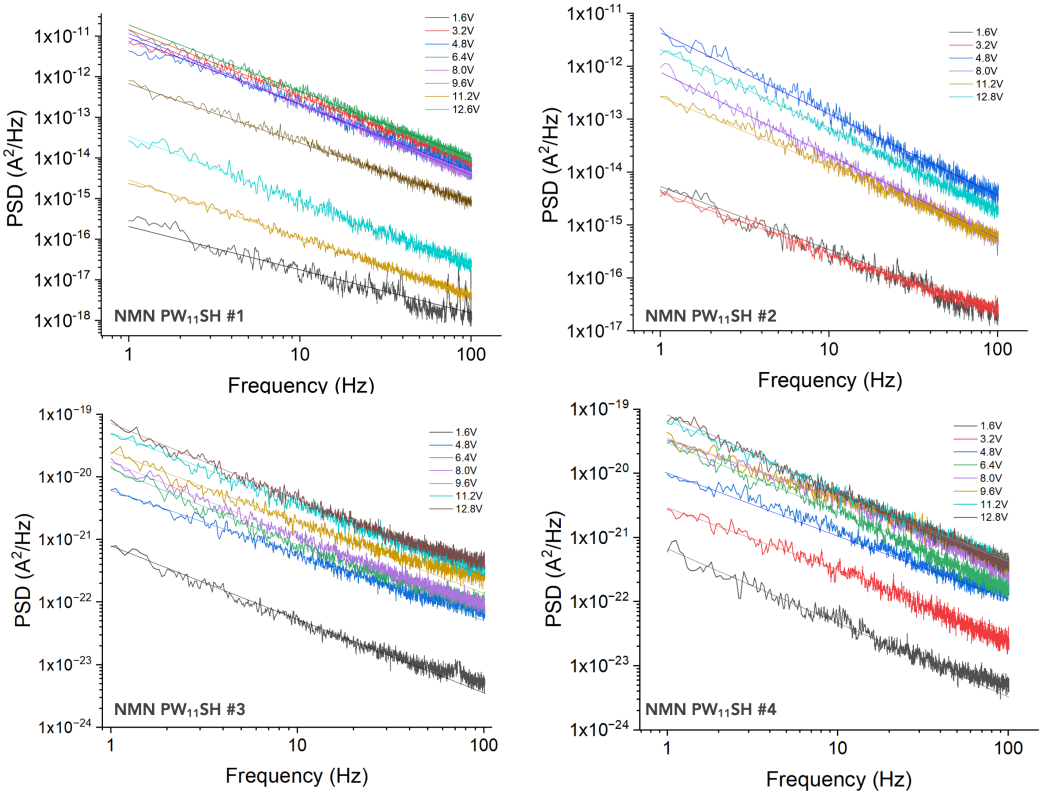

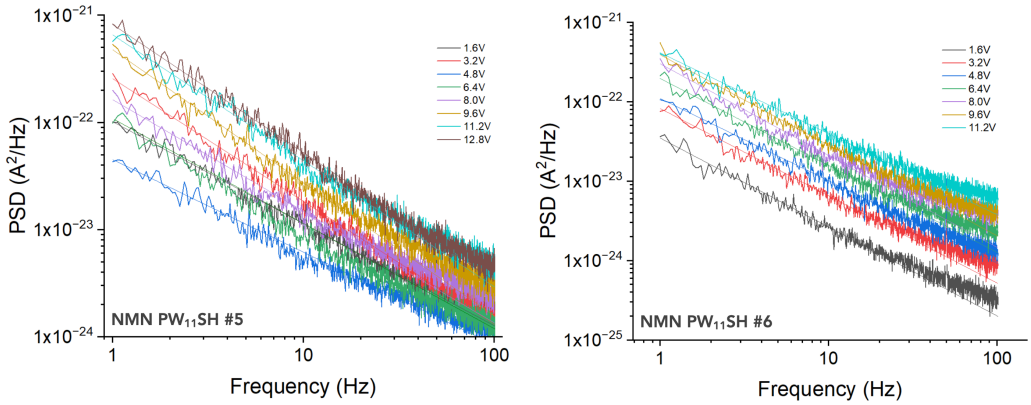

Figure S8. *Current power spectral density (PSD), $S_I(f)$, versus frequency for the $PW_{11}SH$-NMN (batch 1: PEs #1 and #2; batch 2: PEs #3 to #6) measured at several applied voltages.*

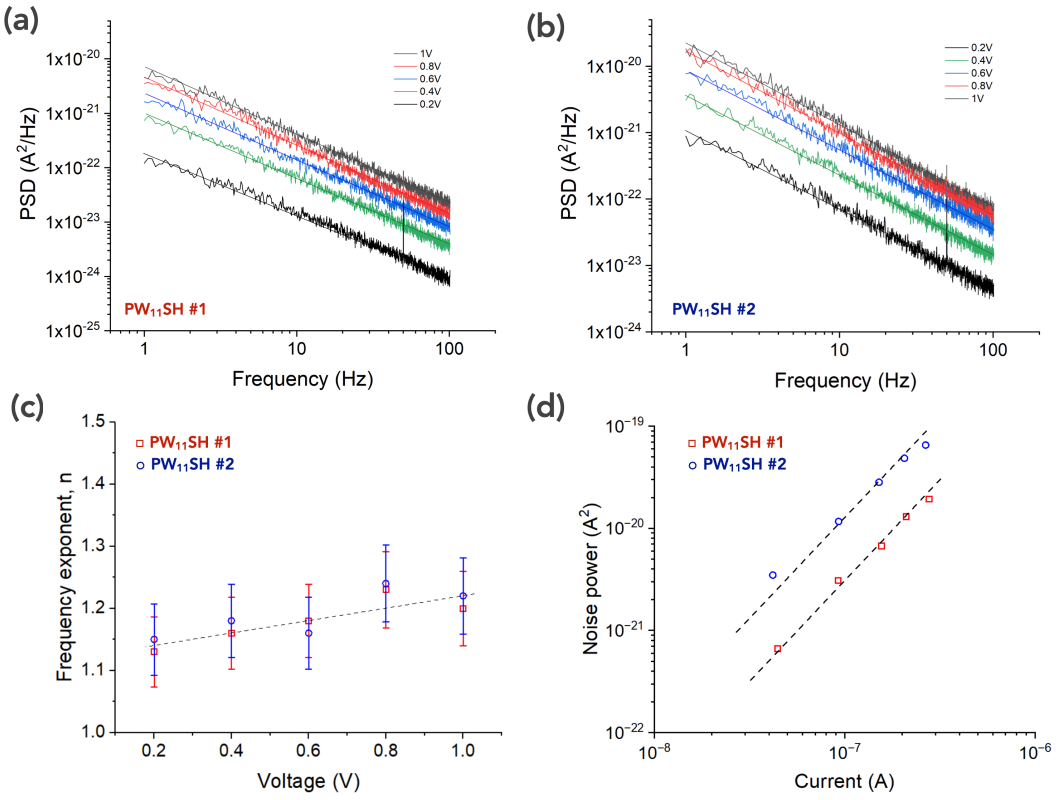

Figure S9. (a-b) *Current power spectral density (PSD) $S_I(f)$, versus frequency for the two PEs of the $PW_{11}SH$-NMN measured at several applied voltages from 0.2*

to 1V. ***(c)*** *Frequency exponent, n, versus the applied voltage. The dashed line is a guide for eyes.* ***(d)*** *Noise power (NoP) versus the DC current. The dashed lines are a guide for the eyes.*

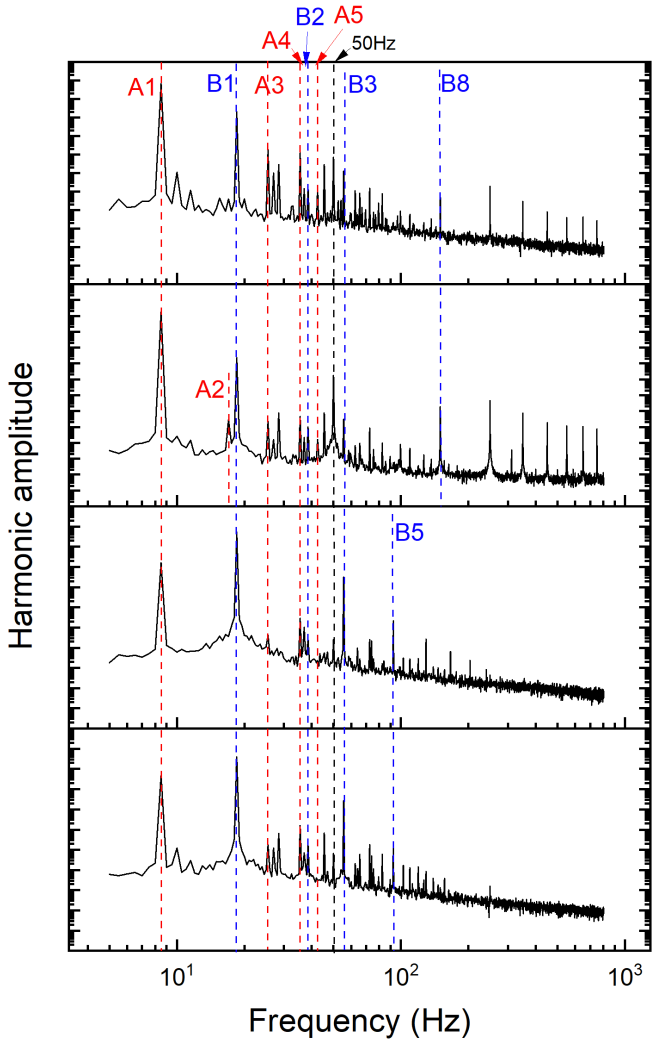

Figure S10*. Two sinusoidal signals, signal A at 8.5 Hz and signal B at 18.5 Hz (peak-to-peak amplitude* V_{PP} *= 2 V for both) are applied at two electrodes of the* PW_{11}*SH-NMN. At the other 4 outputs, the currents are measured by a transimpedance amplifier and fed to the dynamic signal analyzer for FFT analysis. The HHG peaks are labeled as Ai (i = 1 for the fundamental, i = n for the* n^{th} *harmonic, n is an integer) and Bi for harmonics corresponding to the A and B*

input signals, respectively. Only the main HHG are shown for illustration. Peaks in between these integer harmonics correspond to interharmonic distortion and intermodulation distortion (see Ref. 12 for details on the method and analysis procedure). The large number of generated harmonics by the NMNs is the fingerprint of its strongly nonlinear response. The HHG spectra are also different for the 4 outputs, indicating the variability of the building blocks and interactions in the NMN.

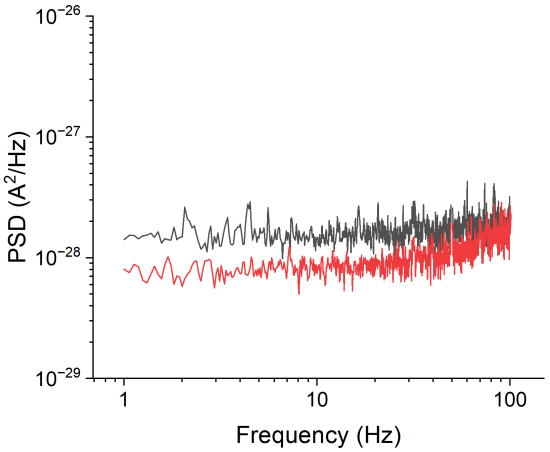

Figure S11. *Noise floor of the setup measured for the two channels (the two trans-impedance amplifiers and the two-channel digital signal analyzer) with the prober tips raised (no sample).*

References

1. G. Yang, W.-S. Chang and D. T. Hallinan, *Journal of Colloid and Interface Science*, 2015, **460**, 164-172.
2. O. Adegoke, K. Takemura and E. Y. Park, *ACS Omega*, 2018, **3**, 1357-1366.
3. F. Wang, C. He, M.-Y. Han, J. Hong Wu and G. Qin Xu, *Chem. Commun.*, 2012, **48**, 6136-6138.
4. Y. Viero, G. Copie, D. Guérin, C. Krzeminski, D. Vuillaume, S. Lenfant and F. Cleri, *The Journal of Physical Chemistry C*, 2015, **119**, 21173-21183.

5. J. Turkevich, P. C. Stevenson and J. Hillier, *Discuss. Faraday Soc.*, 1951, **11**, 55-75.
6. V. Santhanam, J. Liu, R. Agarwal and R. P. Andres, *Langmuir*, 2003, **19**, 7881-7887.
7. V. Santhanam and R. P. Andres, *Nano Letters*, 2004, **4**, 41-44.
8. J. Schindelin, I. Arganda-Carreras, E. Frise, V. Kaynig, M. Longair, T. Pietzsch, S. Preibisch, C. Rueden, S. Saalfeld, B. Schmid, J.-Y. Tinevez, D. J. White, V. Hartenstein, K. Eliceiri, P. Tomancak and A. Cardona, *Nature Methods*, 2012, **9**, 676-682.
9. J. Borges, J. A. Ribeiro, E. M. Pereira, C. A. Carreira, C. M. Pereira and F. Silva, *J Colloid Interface Sci*, 2011, **358**, 626-634.
10. M. Kluenker, M. Mondeshki, M. Nawaz Tahir and W. Tremel, *Langmuir*, 2018, **34**, 1700-1710.
11. Y. Yang, L. A. Serrano and S. Guldin, *Langmuir*, 2018, **34**, 6820-6826.
12. Y. Viero, D. Guérin, A. Vladyka, F. Alibart, S. Lenfant, M. Calame and D. Vuillaume, *Advanced Functional Materials*, 2018, **28**, 1801506.